Stability of disordered topological superconducting phases in magnet-superconductor hybrid systems

Eric Mascot,[1] Chaitra Agrahar,[1] Stephan Rachel,[2] and Dirk K. Morr[1]
[1]*Department of Physics, University of Illinois at Chicago, Chicago, Illinois 60607, USA*
[2]*School of Physics, University of Melbourne, Parkville, VIC 3010, Australia*

(Received 6 May 2019; revised manuscript received 3 October 2019; published 2 December 2019)

Magnet-superconductor hybrid heterostructures constitute a promising candidate system for the quantum engineering of chiral topological superconductivity. Here, we investigate the stability of their topological phases in the presence of various types of potential and magnetic disorder. In particular we consider magnetic disorder in the coupling strength and spin orientation, as well as percolation-type disorder representing missing magnetic moments. We show that potential disorder leads to the weakest suppression of topological phases, while percolation disorder leads to their strongest suppression. In addition, disorder can also lead to the emergence of topological phases in part of the phase diagram that are topologically trivial in a clean system. Moreover, we demonstrate that in the case of correlated potential disorder, the spatial structure of the disorder potential is correlated not only with the particle number density, but also the Chern number density. Finally, we demonstrate how the disorder-induced destruction of topological superconductivity is reflected in the spatial structure and distribution of the Chern number density.

DOI: 10.1103/PhysRevB.100.235102

I. INTRODUCTION

Topological superconductors have attracted much attention in recent years as they represent novel platforms to realize and control Majorana zero modes whose exotic non-Abelian braiding statistics can be employed for the creation of fault-tolerant topological quantum bits [1,2]. Odd-parity spin-triplet superconductors and, in particular, those that possess a chiral p-wave superconducting symmetry [3] represent potential realizations of topological superconductors. Candidate materials which might feature such spin-triplet pairing are Sr_2RuO_4 [4,5], UPt_3 [6], $Cu_xBi_2Se_3$ [7–9], and superfluid ^{3}He [10]. However, most of these materials have been controversially debated [11–13] and the presence of spin-triplet pairing remains to be unambiguously proven.

In addition to these *intrinsic* topological superconductors, there has been growing interest in *artificial* or *engineered* topological superconductors, allowing for the realization of the Kitaev chain [14], the prototype of a one-dimensional (1D) topological superconductor, by proximity-inducing s-wave superconductivity [15] in Rashba nanowires [16–18]. An alternative approach to the creation of Kitaev chains has been taken with magnet-superconductor hybrid (MSH) structures in which (Shiba) chains of magnetic atoms, either via self-assembly [19–22] or via atomic manipulation techniques [23], were placed on the surface of s-wave superconductors. These studies were subsequently extended into two dimensions [24–27] through the creation of magnetic Shiba islands in Pb/Co/Si(111) [28] and Fe/Re(0001)-O(2×1) [29] heterostructures.

One of the defining properties of topological states of matter is their *topological protection* against small perturbations and disorder. On the other hand, the experimental growth of topological materials often leads to significant amounts of disorder, raising the question of what extent of disorder can destroy topological phases. Classical work on disorder effects in intrinsic topological superconductors mainly focused on their bulk properties using continuum Dirac theories [30–33]. More recent studies investigated the stability of the topological surface states in topological superconductors [34,35] or the emergence of Majorana bound states through random-field disorder [36]. In engineered one-dimensional superconductors, impurities and disorder play a particular important role [37–39] because the experimental evidence often relies on the observation of a zero-bias peak associated with the presence of a Majorana bound state [18,20]. Such a zero-bias peak can also be induced by an impurity [40] emphasizing the importance of understanding the effects of disorder on these systems.

MSH heterostructures are particularly suited for the study of disorder effects as disorder can be visualized through scanning tunneling spectroscopy (STS) techniques, which provide simultaneous insight into the topography and spectroscopic (electronic) properties of the constituent magnetic and superconducting subsystems. Indeed, STS experiments measuring the spin-resolved differential conductance have provided evidence for the noncollinear spin structure of Shiba chains [23], while topography scans have revealed the extent of edge disorder in Shiba islands [29]. The question thus naturally arises not only of how disorder affects the topological phase diagram of two-dimensional MSH structures, but also how disorder destroys topological superconducting phases on the microscopic or spatially local level. In this article, we will study these questions by considering the effects of various types of potential and magnetic disorder, and by investigating the spatial correlations between the disorder potential, the

particle density, and the Chern number density, and their relation to the macroscopic topologically invariant of the system, the Chern number.

The paper is organized as follows. In Sec. II we introduce the theoretical model to describe two-dimensional MSH structures, define various types of potential and magnetic disorder, and discuss how the topological phase diagram in the presence of disorder can be computed by using the real space Chern number. In Sec. III we discuss the topological phase diagrams in the presence of random potential and magnetic disorder. In Sec. IV we consider correlated potential disorder, and discuss the spatial correlations between disorder potential, particle density, and Chern number density, and their relation to the macroscopic Chern number. In Sec. V, we present our conclusions.

II. THEORETICAL MODEL

We study the effects of disorder on the topological phase diagram of a two-dimensional MSH structure, also referred to as a Shiba lattice. It is created by placing magnetic adatoms on the surface of a conventional s-wave superconductor possessing a Rashba spin-orbit interaction. The Hamiltonian describing a clean (i.e., nondisordered) Shiba lattice is then given by [25]

$$\begin{aligned} H = & -t\sum_{\mathbf{r},\boldsymbol{\delta}} \psi_{\mathbf{r}}^{\dagger}\tau_z\otimes\sigma_0\psi_{\mathbf{r}+\boldsymbol{\delta}} - \mu\sum_{\mathbf{r}} \psi_{\mathbf{r}}^{\dagger}\tau_z\otimes\sigma_0\psi_{\mathbf{r}} \\ & + i\alpha\sum_{\mathbf{r},\boldsymbol{\delta}} \psi_{\mathbf{r}}^{\dagger}\tau_z\otimes[(\boldsymbol{\sigma}\times\boldsymbol{\delta})\cdot\hat{z}]\psi_{\mathbf{r}+\boldsymbol{\delta}} + \Delta_0\sum_{\mathbf{r}} \psi_{\mathbf{r}}^{\dagger}\tau_x\otimes\sigma_0\psi_{\mathbf{r}} \\ & + J\sum_{\mathbf{r}} \psi_{\mathbf{r}}^{\dagger}\tau_0\otimes(\boldsymbol{S}\cdot\boldsymbol{\sigma})\psi_{\mathbf{r}}, \end{aligned} \tag{1}$$

where $-t$ is the hopping parameter between nearest neighbor sites on a square lattice, $\boldsymbol{\delta}$ is the vector connecting nearest neighbor sites, μ is the chemical potential, α is the Rashba spin-orbit coupling, Δ_0 is the superconducting order parameter, and $\boldsymbol{\sigma}$ and $\boldsymbol{\tau}$ are vectors of Pauli matrices corresponding to spin and Nambu space, respectively. We use the Nambu spinor $\psi_{\mathbf{r}} = (\psi_{\mathbf{r}\uparrow}, \psi_{\mathbf{r}\downarrow}, \psi_{\mathbf{r}\downarrow}^{\dagger}, -\psi_{\mathbf{r}\uparrow}^{\dagger})^T$ where $\psi_{\mathbf{r}\sigma}^{\dagger}$ ($\psi_{\mathbf{r}\sigma}$) creates (annihilates) an electron at site $\mathbf{r}$ and spin σ. The presence of a hard superconducting s-wave gap suppresses the Kondo screening of the magnetic adatoms which allows us to treat the spins classically. For the clean system, we assume a ferromagnetic alignment of all spins along the $\hat{z}$ direction, and therefore set $\boldsymbol{S} = S(0, 0, 1)$ with S being the spin's magnitude. Moreover, due to the particle-hole symmetry of the superconducting state, and the broken time-reversal symmetry arising from the presence of magnetic moments, the topological superconductor belongs to class D [41].

To characterize the topological state of the system in the presence of disorder, which breaks the translational invariance of the system, we compute the topological invariant – the Chern number [42] – in real space using [43–45]

$$C = \frac{1}{2\pi i}\mathrm{Tr}[P[\delta_1 P, \delta_2 P]], \tag{2}$$

with

$$\delta_i P = \sum_{m=-Q}^{Q} c_m e^{-2\pi i m\hat{x}_i/N} P e^{2\pi i m\hat{x}_i/N}, \tag{3}$$

where P is the projector onto the occupied spectrum in real space, N^2 are the number of sites in the system, and c_m are central finite difference coefficients for approximating the partial derivatives. The wave functions and eigenenergies of the system are obtained from a diagonalization of the Hamiltonian, Eq. (1), in real space. Moreover, the coefficients for positive m can be calculated by solving the following linear set of equations for $\boldsymbol{c} = (c_1, \ldots, c_Q)$:

$$\hat{A}\boldsymbol{c} = \boldsymbol{b},\ A_{ij} = 2j^{2i-1},\ b_i = \delta_{i,1},\ i, j \in \{1, \ldots, Q\}, \tag{4}$$

while for negative m, we have $c_{-m} = -c_m$. To achieve a small error in the calculation of the Chern number, we take the largest possible value of Q given by $Q = N/2$. As we show below, important insight into the effects of disorder on the stability of a topological superconductor can be gained by considering the scaled Chern number density, defined as the partial trace over spin and Nambu space, and given by

$$C(\mathbf{r}) = \frac{N^2}{2\pi i}\mathrm{Tr}_{\tau,\sigma}[P[\delta_1 P, \delta_2 P]]_{\mathbf{r},\mathbf{r}}, \tag{5}$$

such that $C = \sum_{\mathbf{r}}[C(\mathbf{r})]/N^2$.

To investigate the effects of disorder on the stability of the topological phases, we consider several types of random potential and magnetic disorder. The random potential disorder is described by the Hamiltonian,

$$H_U = \sum_{\mathbf{r}} U_{\mathbf{r}}\ \psi_{\mathbf{r}}^{\dagger}\tau_z\otimes\sigma_0\psi_{\mathbf{r}}, \tag{6}$$

with $U_{\mathbf{r}} \in [-w_U, w_U]$ being random variables from a uniform probability distribution in the range from $-w_U$ to w_U. Thus, w_U is a measure for the strength of the disorder.

In addition, we consider three different types of magnetic disorder. In the first type, the strength of the magnetic coupling J is disordered, while the spins are still ferromagnetically aligned along the z axis, as described by the Hamiltonian,

$$H_J^{(1)} = \sum_{\mathbf{r}} J_{\mathbf{r}} S\ \psi_{\mathbf{r}}^{\dagger}\tau_0\otimes\sigma_z\psi_{\mathbf{r}}, \tag{7}$$

with $J_{\mathbf{r}}S \in [-w_J, w_J]$ being random variables from a uniform probability distribution. The second type of magnetic disorder is one in which the magnetic coupling J is spatially constant, but the direction of the magnetic moments deviates from the z axis. To describe this type of disorder, we replace the magnetic term in the Hamiltonian, Eq. (1), by

$$H_J^{(2)} = J\sum_{\mathbf{r}} \psi_{\mathbf{r}}^{\dagger}\tau_0\otimes(\boldsymbol{S}_{\mathbf{r}}\cdot\boldsymbol{\sigma})\psi_{\mathbf{r}}, \tag{8}$$

where $\boldsymbol{S}_{\mathbf{r}}$ are spins with random directions which are chosen from a uniform distribution over the spherical cap formed by the polar angle θ. That is, $\boldsymbol{S}_{\mathbf{r}} = S(\sin\theta_{\mathbf{r}}\cos\phi_{\mathbf{r}}, \sin\theta_{\mathbf{r}}\sin\phi_{\mathbf{r}}, \cos\theta_{\mathbf{r}})$ where $\phi_{\mathbf{r}} \in [-\pi, \pi]$, $\theta_{\mathbf{r}} \in [0, \theta]$, and θ thus reflects the extent of the orientational disorder. Finally, the third type of magnetic disorder is of the percolation type, in which the moments are aligned along the

z axis with uniform J, but at each site, there is a probability p that a magnetic moment is missing. We model such a percolation disorder by replacing the magnetic term in the Hamiltonian, Eq. (1), by

$$H_J^{(3)} = JS \sum_{\mathbf{r}} \Theta(w_{\mathbf{r}} - p)\psi_{\mathbf{r}}^{\dagger}\tau_0 \otimes \sigma_z \psi_{\mathbf{r}}, \tag{9}$$

with random variables $w_{\mathbf{r}} \in [0, 1]$ and p describing the degree of percolation, i.e., the mean density of missing magnetic adatoms.

All topological phase diagrams shown below are averaged over n disorder realizations. For each type of disorder, n is determined as the smallest number of disorder realizations for which the following criterion,

$$\frac{\sigma(w, \mu)}{\sqrt{n}} < 0.05, \tag{10}$$

is satisfied for disorder strength w (characterized by w_U, w_J, θ, and p) and chemical potential μ. Here, σ is the standard deviation of the Chern number for a specific w and μ, and for the results shown below, $10 < n < 200$.

In general, the feedback effect of disorder on the electronic structure requires that the local superconducting order parameter $\Delta_{\mathbf{r}}$ be computed self-consistently. In this case, we replace Δ_0 in Eq. (1) with $\Delta_{\mathbf{r}}$ and solve the superconducting gap equation, $\Delta_{\mathbf{r}} = -V\langle c_{\mathbf{r}\downarrow} c_{\mathbf{r}\uparrow}\rangle$, self-consistently in the zero-temperature limit. The value for the pairing interaction V is chosen such that Δ_0 is the homogeneous solution to the gap equation in a clean system. For the topological phase diagrams shown below, we have averaged over between 10 and 200 disorder realizations for every point in the phase diagram. To self-consistently calculate $\Delta_{\mathbf{r}}$ for every disorder realization is computationally prohibitive and beyond our computational resources. We therefore employ a spatially homogeneous superconducting order parameter for most results shown below, and consider the effects of a spatially varying superconducting order parameter on the stability of topological phases in the presence of disorder only in a few select cases. However, we will show that the self-consistent calculation of $\Delta_{\mathbf{r}}$ does not qualitatively change our conclusions regarding the stability of topological phases. Finally, we note that for magnet-superconductor heterostructures with a bulk superconducting substrate, we expect that the feedback effect of disorder on the superconducting order parameter is suppressed by the bulk superconducting order parameter (if the disorder is confined to the surface). However, for two-dimensional systems realized, for instance, in layered superconductors, we expect disorder effects to be much more significant.

III. TOPOLOGICAL PHASES IN THE PRESENCE OF RANDOM POTENTIAL AND MAGNETIC DISORDER

In Figs. 1(a)–1(d), we present the topological Chern number phase diagrams for the four types of disorder introduced in Sec. II as a function of chemical potential μ and disorder strength for a (30×30) site system. For each disorder realization, the Chern number is computed using Eq. (2). We begin by noting that for a clean system (which corresponds to the zero disorder line in all four phase diagrams) in which all spins are ferromagnetically aligned along the z direction, the Shiba

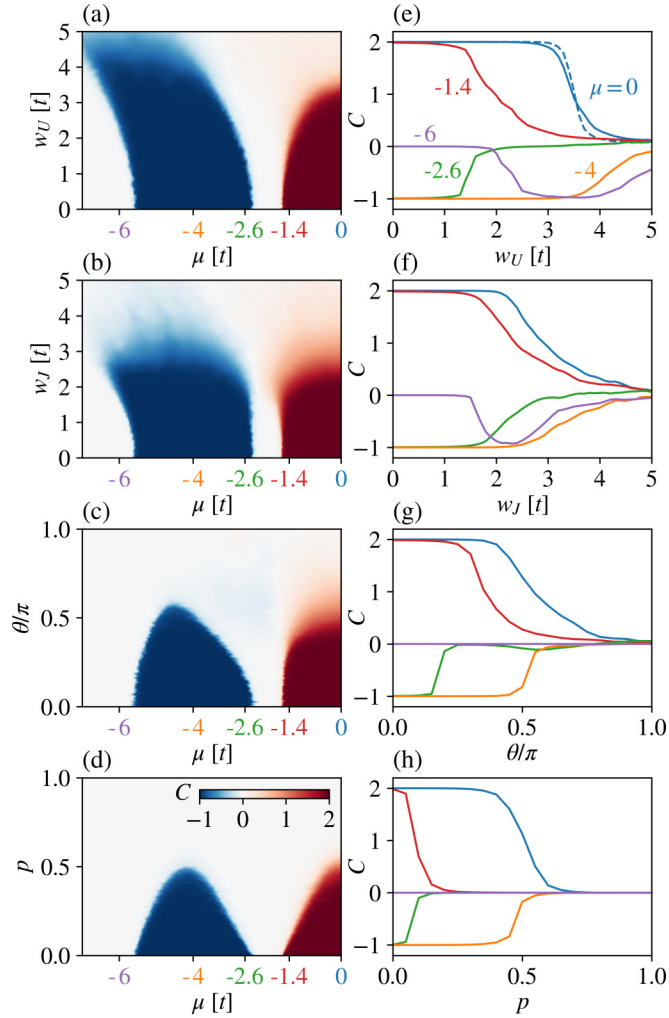

FIG. 1. Topological phase diagram showing the Chern number as a function of chemical potential μ and disorder strength w (as characterized by w_U, w_J, θ, and p) for (a) and (e) potential disorder, described by H_U, and magnetic disorder described by (b) and (f) $H_J^{(1)}$, (c) and (g) $H_J^{(2)}$, and (d) and (h) $H_J^{(3)}$. (e)–(h) Solid lines are line cuts of C in (a)–(d) as a function of disorder strength for chemical potentials $\mu/t = 0, -1.4, -2, -2.6, -4, -6$. The phase diagrams were computed for (30×30) systems with periodic boundary conditions and parameters $(JS, \alpha, \Delta_0) = (2, 0.8, 1.2)t$. Dashed line in (e) was obtained from a (50×50) system.

lattice possesses two topological nontrivial phases with Chern number $C = 2, -1$ that are separated by a trivial phase with $C = 0$ [25]. The transition between these phases occurs when the bulk-gap closes, which for fixed values of JS and Δ_0 yield the following critical chemical potentials [25],

$$\mu_c = \varepsilon \pm \sqrt{(JS)^2 - \Delta_0^2}, \tag{11}$$

where $\varepsilon = 0, \pm 4t$. For the parameters used in Fig. 1, one obtains $\mu_c/t = \pm 1.6,\ \pm 2.4$, and ± 5.6. It immediately follows from Eq. (11) that spatial disorder JS, μ, or Δ_0 can locally tune the system between topological trivial and nontrivial phases.

The phase diagrams in Figs. 1(a)–1(d) reveal that the overall effect of all four types of disorder is similar in that

the topological phases are suppressed with increasing disorder strength. However, the critical disorder strength at which the topological phase collapses depends on the chemical potential: The further the system is located from the critical chemical potential μ_c of the clean system, the larger is the critical disorder strength required to destroy the topological phase. The origin of this dependence lies in the fact that the gap protecting the topological phase increases with increasing distance from μ_c, thus necessitating a larger disorder strength to close it and to drive the system trivial. There are, however, some noteworthy characteristics regarding the effects of the various types of disorder. In particular, we find that the topological phases are more robust against potential disorder than magnetic disorder in J (the latter being described by $H_J^{(1)}$). Moreover, for the case when the spin orientation deviates from the z axis, the topological phases are destroyed when the spin orientation is uniformly distributed over the upper hemisphere (i.e., for $\theta = \pi/2$). Finally, percolation possesses the strongest detrimental effect on the stability of the topological phases. For example, for $\mu = 1.4t$, the topological phase is destroyed by magnetic disorder for $w_J = 2t$ (corresponding to half of the electronic bandwidth), while in the case of percolation, the topological phase is already destroyed for $p \approx 0.1$. Finally, we note that the topological phase diagrams are particle-hole symmetric, i.e., invariant under $\mu \to -\mu$ (see Appendix A).

In Figs. 1(e)–1(h), we present line-cuts of the Chern number with increasing disorder strength for several values of μ [these lines correspond to vertical cuts in Figs. 1(a)–1(d)]. These line-cuts reveal that due to the finite size of the system, the disorder-induced transition between topological and nontopological phases is smooth and continuous, and thus represents a crossover (exhibiting a nonquantized Chern number), rather than a phase transition. However, a comparison of the Chern number line-cuts for different system sizes [see dashed line in Fig. 1(e), which was computed for a (50×50) system] reveals that the transition becomes increasingly sharper and evolves toward a steplike function with increasing system size as expected for a phase transition (the study of larger system sizes, which presumably would exhibit even sharper transitions, is currently beyond our computational abilities). This result suggests that in the thermodynamic limit, a phase transition will occur at a critical value of the disorder strength separating a topological phase with a quantized Chern number, from a nontopological phase with $C = 0$.

While disorder in general leads to the suppression of the topological phases, it can also induce topological phases when the chemical potential is close to the bottom or top of the electronic bands (a similar disorder effect was recently discussed in the context of Chern insulators [46]). For example, for $\mu = -6t$, the clean system is in a gapped, topologically trivial phase with $C = 0$, but enters the topological $C = -1$ phase with increasing nonmagnetic or magnetic disorder [Figs. 1(a) and 1(b)]. This transition is reflected in a qualitative change in the Chern number density $C(\mathbf{r})$ as shown in Figs. 2(a) and 2(b) [the corresponding distribution of $C(\mathbf{r})$ for these two cases is presented in Fig. 2(c)]. While for $w_U = 2t$ [Fig. 2(a)], the distribution of $C(\mathbf{r})$ is centered around zero (leading to a nearly vanishing Chern number), the distribution for $w_U = 3t$ [Fig. 2(b)] is significantly broader and shifted to lower values,

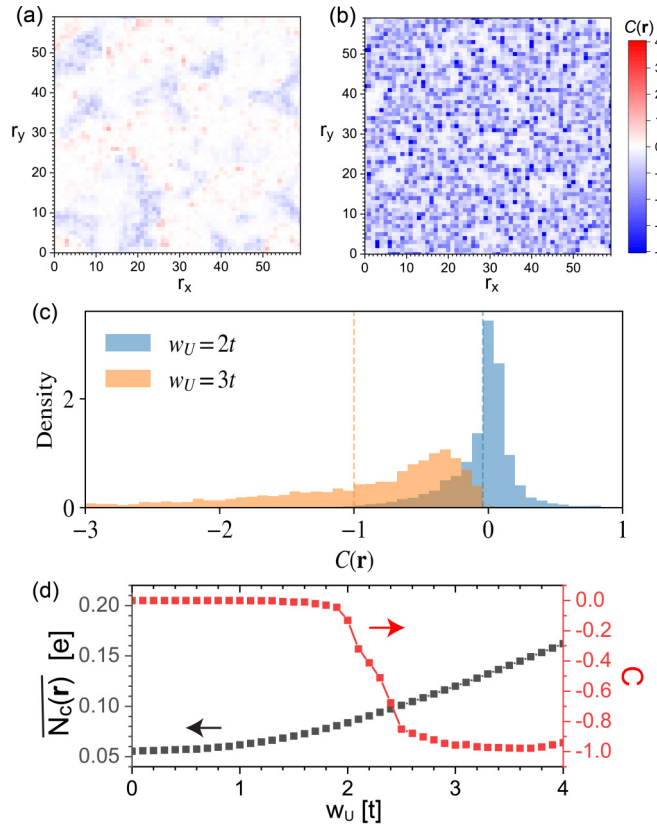

FIG. 2. Spatial plots of the Chern number density $C(\mathbf{r})$ for a 60×60 system for the case of potential disorder with $\mu = -6t$ and (a) $w_U = 2t$, and (b) $w_U = 3t$. (c) Distributions of the Chern number density $C(\mathbf{r})$ for the two cases shown in (a) and (b). The vertical dashed lines in (c) show the mean values of the distribution, corresponding to the macroscopic Chern numbers. The histograms are scaled such that the integral over the histogram is equal to unity. (d) Spatially averaged charge density $\overline{N_c(\mathbf{r})}$ and Chern number as a function of w_U. Parameters are $(JS, \alpha, \Delta) = (2.0, 0.8, 1.2)t$.

resulting in a Chern number of $C = -1$. It is interesting to note that despite the significant width of the distribution for $w_U = 3t$, the Chern number is quantized with high numerical accuracy within 0.0007%. This disorder-induced topological phase arises from a disorder-induced increase in the charge density with increasing disorder strength [see Fig. 2(d)], which is of particular importance when the chemical potential is near the bottom or top of the band where the charge density is low in the clean system. Indeed, this increase in the charge density moves the effective chemical potential away from the bottom/top of the bands, into the topological region of the phase diagram, thus resulting in an emergence of a topological phase with increasing disorder strength [see Fig. 2(d)].

A similar disorder-induced topological phase also emerges for magnetic disorder described by $H_J^{(1)}$ in the trivial region of the phase diagram between the $C = 2$ and $C = -1$ phases. For example, for $\mu = -1.8t$ (which corresponds to the topological trivial phase in the clean limit) a transition from a trivial to a topological phase occurs between $w_J = t$ and $w_J = 2t$. Starting from the clean limit, we find that with increasing w_J, the Chern number density becomes disordered [Fig. 3(a) for $w_J = t$], but its distribution [Fig. 3(c)], while increasing

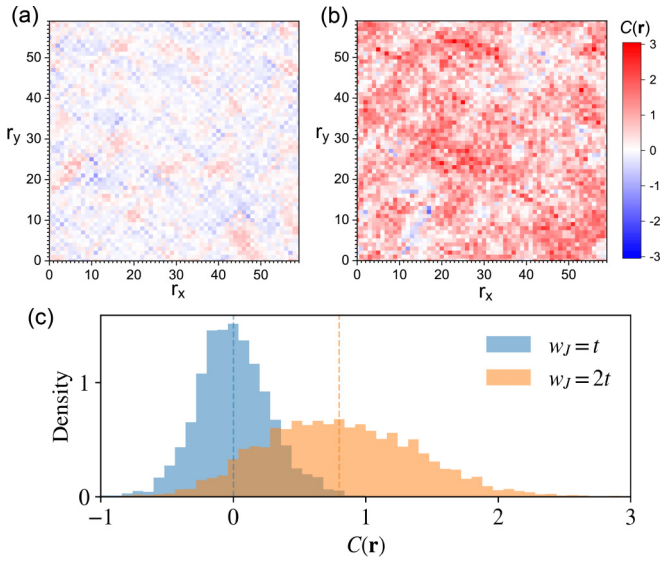

FIG. 3. Spatial plots of $C(\mathbf{r})$ for the case of magnetic disorder described by $H_J^{(1)}$ with $\mu = -1.8t$ and (a) $w_J = t$ and (b) $w_J = 2t$. (c) Distributions of the Chern number density $C(\mathbf{r})$ for the two cases shown in (a) and (b). The vertical dashed lines in (c) show the mean values of the distribution, corresponding to the macroscopic Chern numbers. The histograms are scaled such that the integral over the histogram is equal to unity. Parameters are $(JS, \alpha, \Delta) = (2.0, 0.8, 1.2)t$.

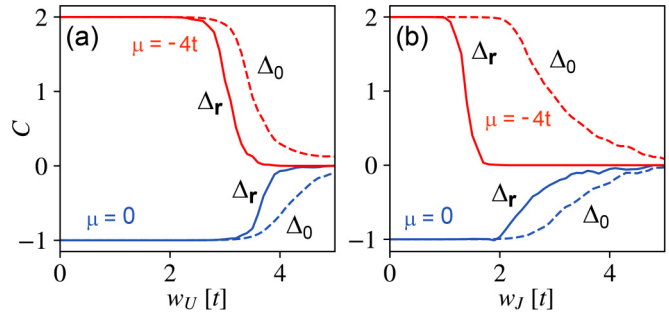

FIG. 4. The Chern number as a function of disorder strength w for (a) potential disorder described by H_U, and (b) magnetic disorder described by $H_J^{(1)}$ for chemical potentials $\mu = -4t, 0$. Solid lines use the self-consistently solved superconducting order parameter $\Delta_\mathbf{r}$ and dashed lines use a homogenous superconducting order parameter Δ_0. The Chern numbers were computed for a (30×30) system with periodic boundary conditions and parameters $(JS, \alpha, \Delta) = (2.0, 0.8, 1.2)t$.

in width, remains centered around zero. On the other hand, for $w_J = 2t$ [Fig. 3(b)], the distribution of $C(\mathbf{r})$ moves to higher values, resulting in a Chern number of $C = 0.8$ for a 60×60 system. Note that with increasing system size, the Chern number moves closer to its quantized value of $C = 2$: for a 30×30 system, we find $C = 0.67$, while for a 60×60 system we have $C = 0.8$. This disorder-induced topological phase transition can be understood as follows: According to Eq. (11), local variations in J will lead to local variations in μ_c, which implies that even for $\mu = -1.8t$, the system can be locally in a topological phase, if $J_\mathbf{r}S$ is sufficiently large. Thus, with increasing $J_\mathbf{r}S$, larger and larger parts of the system become locally topological, eventually resulting in the transition to a topological superconducting phase.

We next consider the feedback effects of disorder on the local electronic structure by self-consistently computing the superconducting order parameter, as discussed in Sec. II. To ascertain the effect on the stability of topological phases, we compare in Fig. 4 the Chern number as a function of magnetic and nonmagnetic disorder strength (described by H_U and $H_J^{(1)}$, respectively) for a constant superconducting order parameter Δ_0, and for a self-consistently computed order parameter $\Delta_\mathbf{r}$ (in the absence of disorder, $\Delta_0 = \Delta_\mathbf{r}$), for two values of the chemical potential μ. In both cases, we find that the topological phase is more quickly suppressed with increasing disorder strength when the superconducting order parameter is self-consistently computed, with this effect being significantly weaker for potential [Fig. 4(a)] than for magnetic disorder [Fig. 4(b)]. In general, we find that this stronger suppression is more quantitative than qualitative in nature, and therefore does not affect the general conclusions of Fig. 1.

Finally, we note with regards to the set of parameters used in Fig. 1 and below, that while the emergence of topological phases requires $J > \Delta$ [see Eq. (11)], they exist for any $\alpha > 0^+$. However, our numerical studies have shown that a sizable superconducting gap (which protects the topological phase) of the order of the input superconducting order parameter Δ_0 emerges only for $\alpha \gtrsim 0.1J$. Specifically, the parameters used in Fig. 1 were chosen to facilitate the calculation of the Chern number and Chern number density (which is computationally more demanding for small superconducting gaps), and to obtain phase diagrams in which the topological phases are extended over larger ranges of μ for demonstration purposes. However, the qualitative nature of the results shown in Fig. 1 as well as the conclusions we have drawn remain valid also for other sets of parameters as shown in Appendix B.

IV. TOPOLOGICAL PHASES IN THE PRESENCE OF CORRELATED POTENTIAL DISORDER

To understand how disorder leads to the collapse of topological phases, it is instructive to consider the spatial correlations between the local disorder, the particle number density, and the Chern number density. To this end, we consider a spatially correlated potential disorder that allows for the emergence of larger domains of nearly the same disorder potential, which facilitates the spatial comparison. As before we start by considering a random potential disorder, as described by Eq. (6), but then replace $U_\mathbf{r}$ by the disorder $\overline{U}_\mathbf{r}$ which is generated from $U_\mathbf{r}$ by using a low-pass filter via

$$\overline{U}_\mathbf{r} = \mathcal{F}_\mathbf{r}^{-1}\left[\mathcal{F}_\mathbf{k}[U_\mathbf{r}]e^{-\mathbf{k}^2/\mathbf{K}_c^2}\right], \tag{12}$$

where $\mathcal{F}$ is the Fourier transform over $\mathbf{r}$ and $\mathbf{K}_c$ is the cutoff wave vector. This low-pass filter implies that the short-wavelength fluctuations in the disorder potential $U_\mathbf{r}$ with wave number $k > |\mathbf{K}_c|$ are eliminated, which smoothes the disorder potential and increases the disorder correlations as described by

$$\rho_\delta = \frac{\langle \overline{U}_\mathbf{r}\overline{U}_{\mathbf{r}+\delta}\rangle - \mu_U^2}{\sigma_U^2}, \tag{13}$$

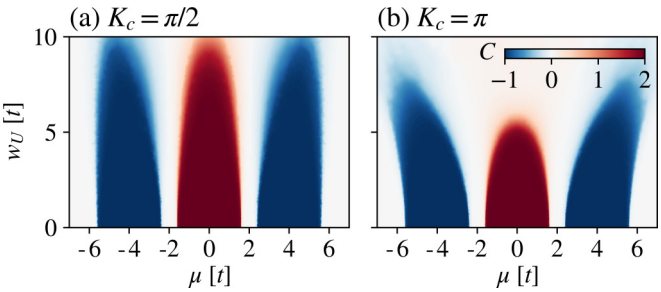

FIG. 5. Topological phase diagram for correlated potential disorder [see Eq. (12)] with (a) $|\mathbf{K}_c| = \pi/2$ and (b) $|\mathbf{K}_c| = \pi$. The phase diagrams were obtained for the same parameters as those in Fig. 1.

where the mean value $\mu_U = \langle \overline{U}_\mathbf{r} \rangle \equiv 0$, and the variance is $\sigma_U^2 = \langle (\overline{U}_\mathbf{r})^2 \rangle$. For random disorder (corresponding to $|\mathbf{K}_c| = \infty$), we obtain for nearest neighbor correlations (i.e, $\boldsymbol{\delta} = \hat{x}, \hat{y}$) $\rho_{\hat{x}} \leqslant 10^{-6}$ (which vanishes in the thermodynamic limit). In contrast, for the case $|\mathbf{K}_c| = \pi$, which we consider below as an example for correlated disorder, we have $\rho_{\hat{x}} \approx 0.04$. This implies that the disorder potential develops short-range correlations with decreasing $|\mathbf{K}_c|$, as the systems begins to exhibit larger domains of the same potential.

In Fig. 5, we present the topological phase diagrams for correlated potential disorder, as described by Eq. (12) with $|\mathbf{K}_c| = \pi/2$ and π. We used the same parameters as in Fig. 1 and can thus directly compare the phase diagrams for random and correlated disorder. We find that correlated disorder possesses a weaker effect on the stability of the topological phases than random potential disorder, requiring thus an increasingly larger critical disorder strength (with decreasing $|\mathbf{K}_c|$) to destroy the topological phases.

To further elucidate the nature of the disorder-driven transition from a topological to a trivial phase, and the resulting critical disorder strength, we present in Figs. 6(a) and 6(b) the evolution of the lowest energy eigenstates and the Chern number with increasing w_U for correlated potential disorder with $|\mathbf{K}_c| = \pi$. The critical disorder strength, defined as that disorder strength where the first eigenstate reaches zero energy, is given by $w_U^c \approx 1.8t$. w_U^c varies between different disorder realizations, and possesses a disorder-averaged value (using $n = 50$ disorder realizations) of $\langle w_U^c \rangle \approx 2.0$. While the Chern number stays approximately quantized for $w_U < w_U^c$, it is substantially reduced from its value $C = -1$ in the clean system for $w_U > w_U^c$. To understand how this departure from $C = -1$ occurs, we present in Figs. 6(c) and 6(d) a spatial plot of $C(\mathbf{r})$ for $w_U = 0.5t$ and $w_U = 1.5t$, respectively; for both values $w_U < w_U^c$. As expected, we find that disorder results in an inhomogeneous spatial form of $C(\mathbf{r})$ and that with increasing disorder strength, the spatial variations in $C(\mathbf{r})$ increase as well. This can be visualized by plotting a histogram of $C(\mathbf{r})$ [see Fig. 6(e)] which shows that increasing the disorder strength leads to a broadening of the $C(\mathbf{r})$ distribution. However, only for $w_U > w_U^c$ does the entire distribution shift to lower values [see $w_U = 2.0t$ in Fig. 6(e)], resulting in a decrease of the Chern number. For $w_U \gg w_U^c$ [see $w_U = 5.0t$ in Fig. 6(e)], the distribution becomes centered around zero, leading to a vanishing Chern number.

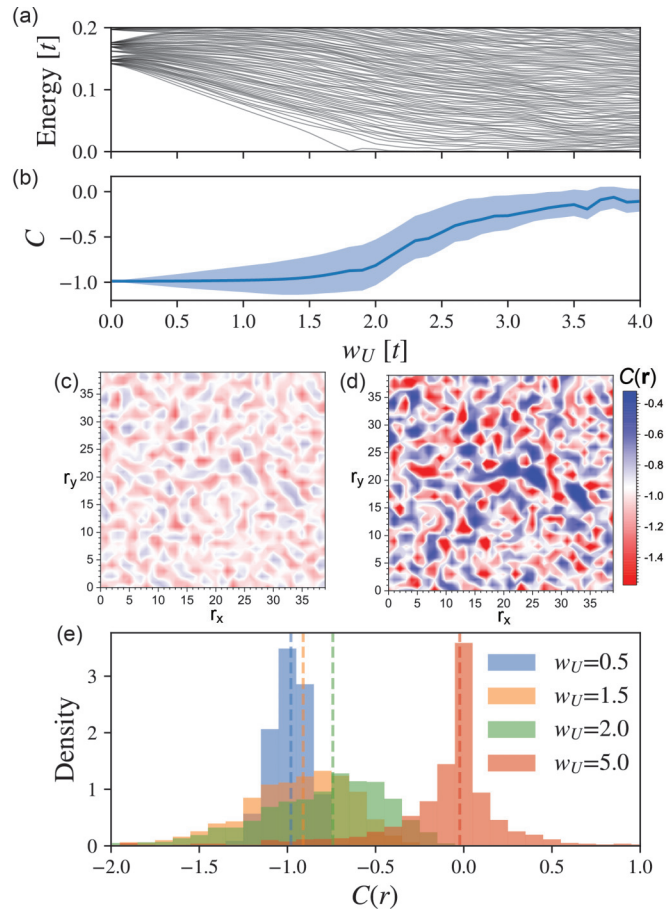

FIG. 6. Evolution of (a) the lowest energy eigenstates, and (b) the Chern number and the upper and lower quartiles (light blue area) of the Chern number density with increasing disorder strength w_U for $|\mathbf{K}_c| = \pi$ and $\mu = -4t$, corresponding to the $C = -1$ phase in the clean limit. The critical disorder value is given by $w_U^c \approx 1.8t$ for this particular disorder realization. Spatial plot of the Chern number density $C(r)$ for (c) $w_U = 0.5t$ and (d) $w_U = 1.5t$. (e) Distributions of the Chern number density $C(\mathbf{r})$ for different values of disorder strength w_U. The vertical dashed lines show the mean values of the distribution, corresponding to the macroscopic Chern numbers. These results were obtained for a (40×40) system with parameters $(JS, \alpha, \Delta) = (0.5, 0.2, 0.3)t$.

To investigate the correlations of the spatial structure of $C(\mathbf{r})$ with other physical observables in the system, we consider the Pearson correlation function between two physical observables $X(\mathbf{r})$ and $Y(\mathbf{r})$ defined via

$$\rho_{X,Y} = \left\langle \frac{X(\mathbf{r}) - \mu_X}{\sigma_X} \frac{Y(\mathbf{r}) - \mu_Y}{\sigma_Y} \right\rangle, \tag{14}$$

where μ_i, σ_i $(i = X, Y)$ are the expectation value and standard deviation of the observable i. In Fig. 7(a), we present the correlation functions for the disorder potential, $\overline{U}_\mathbf{r}$, the particle density $N_\mathbf{r}$, and the Chern number density $C(\mathbf{r})$. As expected, we find that $\overline{U}_\mathbf{r}$ and $N_\mathbf{r}$ are nearly completely anticorrelated, with a local increase in $\overline{U}_\mathbf{r}$ (i.e., creating a repulsive potential) leading to a decrease in $N_\mathbf{r}$. Interestingly enough, we find that there also exists a substantial correlation between $C(\mathbf{r})$ and $\overline{U}_\mathbf{r}$, and thus also between $C(\mathbf{r})$ and $N_\mathbf{r}$. This is also

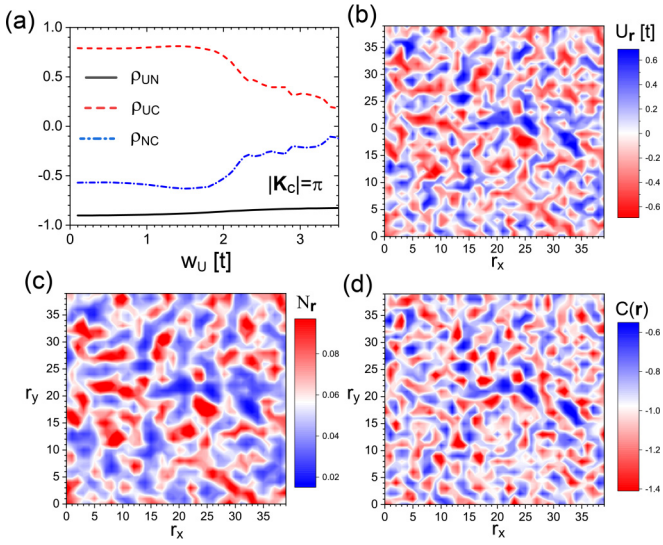

FIG. 7. (a) Pearson correlation $\rho_{X,Y}$ for the disorder potential $\overline{U}_{\mathbf{r}}$ (denoted by U), the particle density $N_{\mathbf{r}}$ (denoted by N), and the Chern number density $C(\mathbf{r})$ (denoted by C). Spatial plot of (b) $\overline{U}_{\mathbf{r}}$, (c) $N_{\mathbf{r}}$, and (d) $C(\mathbf{r})$ for $w_U = 1.5t$.

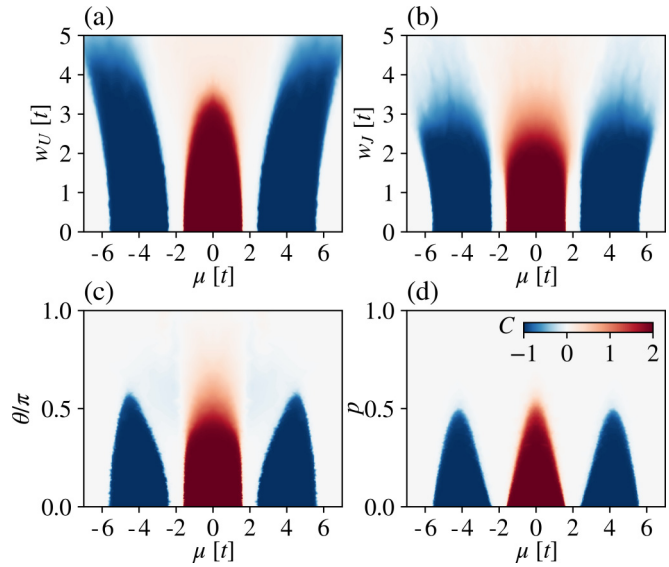

FIG. 8. Topological phase diagram showing the Chern number as a function of chemical potential μ, and disorder strength w (as characterized by w_U, w_J, θ, and p) for (a) potential disorder described by H_U, and magnetic disorder described by (b) $H_J^{(1)}$, (c) $H_J^{(2)}$, and (d) $H_J^{(3)}$. The phase diagrams were computed for a (30×30) system with periodic boundary conditions and parameters $(JS, \alpha, \Delta_0) = (2, 0.8, 1.2)t$.

evident from a comparison of the spatial form of $\overline{U}_{\mathbf{r}}$, $N_{\mathbf{r}}$, and $C(\mathbf{r})$, shown in Figs. 7(b)–7(d) for the case of $w_U = 1.5t$. All three properties possess to a large extent the same spatial structure, in agreement with the substantial correlation revealed by $\rho_{X,Y}$ shown in Fig. 7(a). This result might open a new approach to investigating the form of the Chern number density, and hence the Chern number, in real space, through measurements, for example, of the particle number density. The latter can in general be obtained from scanning tunneling microscopy (STM) experiments which measure the local, i.e., spatially resolved, differential conductance, $dI(\mathbf{r}, V)/dV$. For one-band models (such as the one considered here), dI/dV is proportional to the density of states, such that the particle number density (at $T = 0$) can be obtained from

$$N_{\mathbf{r}} \sim \int_{-\infty}^{0} dV \frac{I(\mathbf{r}, V)}{dV}. \tag{15}$$

For details, and a discussion of the differential conductance in multiband systems, see Ref. [47]. Finally, we note that the Pearson correlations between the Chern number density and the spin density (or the spin-resolved charge density) are similar to those shown in Fig. 7, as shown in Appendix C.

V. CONCLUSIONS

We have investigated the effects of various types of potential and magnetic disorder on the stability of topological superconductivity in two-dimensional magnet-superconductor hybrid systems. These hybrid structures are of great current interest as they represent a promising platform for engineering Majorana fermions. We showed that random potential disorder leads to the weakest, while percolation disorder leads to the strongest suppression of topological superconducting phases. However, both magnetic and potential disorder can also lead to the emergence of topological phases in part of the phase diagram that are topologically trivial in a clean system. We also demonstrated that spatially correlated potential disorder exerts a weaker effect on the topological phase diagram than random disorder. Moreover, we showed that disorder leads to a spatially inhomogeneous form of the Chern number density, the width of whose distribution increases with increasing disorder. We also demonstrated that the disorder-induced phase transition from topological to trivial phases is accompanied by a downward shift of the distribution of the Chern number density, becoming centered around zero, and leading to a vanishing mean, i.e., macroscopic Chern number. However, even in the topological trivial phase, spatial domains of nonzero Chern number density remain. Finally, we showed that there exist considerable spatial correlations between the spatial structure of the Chern number density, the potential disorder, and the particle number density. This result might open a new approach to detecting the Chern number density, and hence the Chern number, in real space through measurements of the particle density.

ACKNOWLEDGMENTS

This work was supported by the US Department of Energy, Office of Science, Basic Energy Sciences, under Grant No. DE-FG02-05ER46225 (E.M., C.A., and D.K.M.). S.R. acknowledges support from an Australian Research Council Future Fellowship (Grant No. FT180100211).

APPENDIX A: PARTICLE-HOLE SYMMETRY OF THE TOPOLOGICAL DISORDER PHASE DIAGRAM

In Fig. 8 we present the topological phase diagrams for the four types of disorder discussed above over the entire range of chemical potential $-7t \leqslant \mu \leqslant 7t$. As mentioned in the

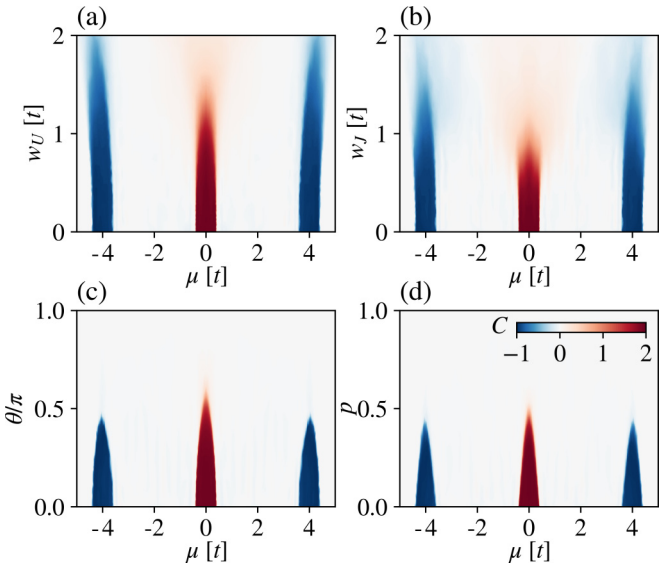

FIG. 9. Topological phase diagram showing the Chern number as a function of chemical potential μ, and disorder strength w (as characterized by w_U, w_J, θ, and p) for (a) potential disorder described by H_U, and magnetic disorder described by (b) $H_J^{(1)}$, (c) $H_J^{(2)}$, and (d) $H_J^{(3)}$. The phase diagrams were computed for a (30×30) system with periodic boundary conditions and parameters $(JS, \alpha, \Delta) = (0.5, 0.2, 0.3)t$.

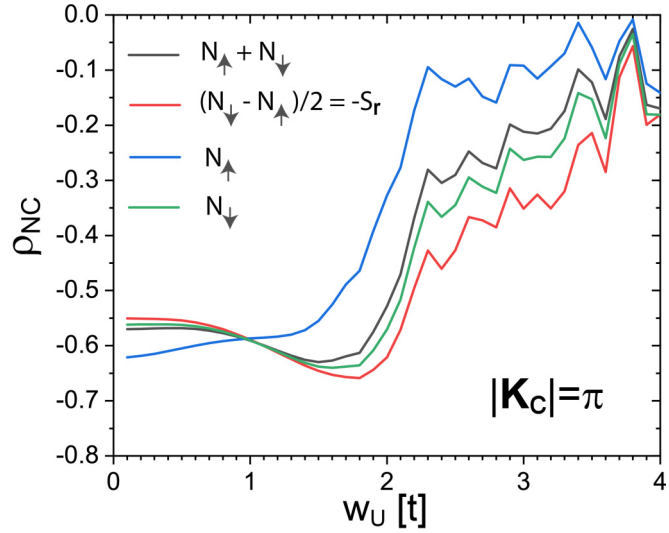

FIG. 10. Pearson correlation ρ_{NC} for the disorder potential $\overline{U}_\mathbf{r}$ (denoted by U), and $N_\mathbf{r}$ (denoted by N) with $N = N_\uparrow + N_\downarrow$ (black line), $N = (N_\downarrow - N_\uparrow)/2 = -S_\mathbf{r}$ (red line), $N = N_\uparrow$ (blue line), and $N = N_\downarrow$ (green line). Here, $N_{\uparrow,\downarrow}$ describes the spin-resolved particle density for the spin-↑ and spin-↓ electrons, respectively.

discussion of Fig. 1 above, the phase diagram is particle-hole symmetric, i.e., invariant under the exchange $\mu \to -\mu$.

APPENDIX B: PHASE DIAGRAM FOR SMALL PARAMETERS

To demonstrate that the above results for the effects of disorder on the topological phase diagram are general, and not specific to a particular set of parameters, we present in Fig. 9 the topological phase diagrams for a set of smaller parameters. We note that the smaller effective superconducting gap arising from this set of parameters renders the calculation of the Chern number much more demanding computationally. We find that this set of parameters leads to the same conclusion as discussed above. In particular, we find the same disorder-induced topological phase discussed in the context of Fig. 1.

APPENDIX C: CORRELATION BETWEEN THE CHERN NUMBER DENSITY AND THE SPIN DENSITY

In Fig. 7 we showed that there exist considerable correlations between the Chern number density and the particle density in the presence of correlated potential disorder. Due to the broken SU(2) spin symmetry of the MSH structure, the question arises whether more insight can be gained by considering the correlations between the Chern number density and the spin-resolved particle density, $N_{\uparrow,\downarrow}(\mathbf{r})$, or the spin density $S_\mathbf{r} = (N_\uparrow(\mathbf{r}) - N_\downarrow(\mathbf{r}))/2$. In Fig. 10 we present the Pearson correlation function between the Chern number density and the spin-resolved quantities, which shows the same qualitative, and to a large extent, quantitative behavior, as that between $C(\mathbf{r})$ and the total particle density $N(\mathbf{r}) = N_\uparrow(\mathbf{r}) + N_\downarrow(\mathbf{r})$ considered in Fig. 7.

[1] C. Nayak, S. H. Simon, A. Stern, M. Freedman, and S. Das Sarma, Rev. Mod. Phys. **80**, 1083 (2008).
[2] S. D. Sarma, M. Freedman, and C. Nayak, npj Quant. Inform. **1**, 15001 (2015).
[3] N. Read and D. Green, Phys. Rev. B **61**, 10267 (2000).
[4] Y. Maeno, H. Hashimoto, K. Y. S. Nishizaki, T. Fujita, J. G. Bednorz, and F. Lichtenberg, Nature (London) **372**, 532 (1994).
[5] A. P. Mackenzie and Y. Maeno, Rev. Mod. Phys. **75**, 657 (2003).
[6] R. Joynt and L. Taillefer, Rev. Mod. Phys. **74**, 235 (2002).
[7] Y. S. Hor, A. J. Williams, J. G. Checkelsky, P. Roushan, J. Seo, Q. Xu, H. W. Zandbergen, A. Yazdani, N. P. Ong, and R. J. Cava, Phys. Rev. Lett. **104**, 057001 (2010).
[8] S. Sasaki, M. Kriener, K. Segawa, K. Yada, Y. Tanaka, M. Sato, and Y. Ando, Phys. Rev. Lett. **107**, 217001 (2011).
[9] K. Matano, M. Kriener, K. Segawa, Y. Ando, and G. qing Zheng, Nat. Phys. **12**, 852 (2016).
[10] G. E. Volovik, *The Universe in a Helium Droplet* (Oxford University Press, Oxford, 2003).
[11] C. Kallin and J. Berlinsky, Rep. Prog. Phys. **79**, 054502 (2016).
[12] M. Sato and Y. Ando, Rep. Prog. Phys. **80**, 076501 (2017).
[13] A. P. Mackenzie, T. Scaffidi, C. W. Hicks, and Y. Maeno, npj Quant. Mat. **2**, 40 (2017).
[14] A. Y. Kitaev, Phys. Usp. **44**, 131 (2001).
[15] L. Fu and C. L. Kane, Phys. Rev. Lett. **100**, 096407 (2008).
[16] R. M. Lutchyn, J. D. Sau, and S. Das Sarma, Phys. Rev. Lett. **105**, 077001 (2010).
[17] Y. Oreg, G. Refael, and F. von Oppen, Phys. Rev. Lett. **105**, 177002 (2010).

[18] V. Mourik, K. Zuo, S. M. Frolov, S. R. Plissard, E. P. A. M. Bakkers, and L. P. Kouwenhoven, Science **336**, 1003 (2012).
[19] S. Nadj-Perge, I. K. Drozdov, B. A. Bernevig, and A. Yazdani, Phys. Rev. B **88**, 020407(R) (2013).
[20] S. Nadj-Perge, I. K. Drozdov, J. Li, H. Chen, S. Jeon, J. Seo, A. H. MacDonald, B. A. Bernevig, and A. Yazdani, Science **346**, 602 (2014).
[21] M. Ruby, F. Pientka, Y. Peng, F. von Oppen, B. W. Heinrich, and K. J. Franke, Phys. Rev. Lett. **115**, 197204 (2015).
[22] R. Pawlak, M. Kisiel, J. Klinovaja, T. Meier, S. Kawai, T. Glatzel, D. Loss, and E. Meyer, npj Quant. Inf. **2**, 16035 (2016).
[23] H. Kim, A. Palacio-Morales, T. Posske, L. Rozsa, K. Palotas, L. Szunyogh, M. Thorwart, and R. Wiesendanger, Sci. Adv. **4**, 5251 (2018).
[24] M. Sato, Y. Takahashi, and S. Fujimoto, Phys. Rev. B **82**, 134521 (2010).
[25] J. Li, T. Neupert, Z. Wang, A. H. MacDonald, A. Yazdani, and B. A. Bernevig, Nat. Commun. **7**, 12297 (2016).
[26] J. Röntynen and T. Ojanen, Phys. Rev. Lett. **114**, 236803 (2015).
[27] S. Rachel, E. Mascot, S. Cocklin, M. Vojta, and D. K. Morr, Phys. Rev. B **96**, 205131 (2017).
[28] G. C. Ménard, S. Guissart, C. Brun, R. T. Leriche, M. Trif, F. Debontridder, D. Demaille, D. Roditchev, P. Simon, and T. Cren, Nat. Commun. **8**, 2040 (2017).
[29] A. Palacio-Morales, E. Mascot, S. Cocklin, H. Kim, S. Rachel, D. K. Morr, and R. Wiesendanger, Sci. Adv. **5**, 6600 (2019).
[30] A. W. W. Ludwig, M. P. A. Fisher, R. Shankar, and G. Grinstein, Phys. Rev. B **50**, 7526 (1994).
[31] T. Senthil and M. P. A. Fisher, Phys. Rev. B **61**, 9690 (2000).
[32] M. S. Foster, H.-Y. Xie, and Y.-Z. Chou, Phys. Rev. B **89**, 155140 (2014).
[33] F. Evers and A. D. Mirlin, Rev. Mod. Phys. **80**, 1355 (2008).
[34] R. Queiroz and A. P. Schnyder, Phys. Rev. B **89**, 054501 (2014).
[35] R. Queiroz and A. P. Schnyder, Phys. Rev. B **91**, 014202 (2015).
[36] T. Zhou, Sci. Rep. **7**, 13811 (2017).
[37] P. W. Brouwer, M. Duckheim, A. Romito, and F. von Oppen, Phys. Rev. B **84**, 144526 (2011).
[38] O. A. Awoga, K. Björnson, and A. M. Black-Schaffer, Phys. Rev. B **95**, 184511 (2017).
[39] J. T. Ren, H. F. Lü, S. S. Ke, Y. Guo, and H. W. Zhang, Beilstein J. Nanotechnol. **9**, 1358 (2018).
[40] D. Bagrets and A. Altland, Phys. Rev. Lett. **109**, 227005 (2012).
[41] S. Ryu, A. P. Schnyder, A. Furusaki, and A. W. Ludwig, New J. Phys. **12**, 065010 (2010).
[42] D. J. Thouless, M. Kohmoto, M. P. Nightingale, and M. den Nijs, Phys. Rev. Lett. **49**, 405 (1982).
[43] E. Prodan, T. L. Hughes, and B. A. Bernevig, Phys. Rev. Lett. **105**, 115501 (2010).
[44] E. Prodan, *A Computational Non-commutative Geometry Program for Disordered Topological Insulators*, Vol. 23 (Springer Briefs in Mathematical Physics, Cambridge, 2017).
[45] E. Prodan, J. Phys. A: Math. Theor. **44**, 113001 (2011).
[46] Y. Kuno, Phys. Rev. B **100**, 054108 (2019).
[47] D. K. Morr, Rep. Prog. Phys. **80**, 014502 (2017).